NANO LETTERS

Letter

pubs.acs.org/NanoLett

High Efficiency Solid-State Sensitized Solar Cell-Based on Submicrometer Rutile TiO_2 Nanorod and $CH_3NH_3PbI_3$ Perovskite Sensitizer

Hui-Seon Kim,[†] Jin-Wook Lee,[†] Natalia Yantara,[‡] Pablo P. Boix,[‡] Sneha A. Kulkarni,[‡] Subodh Mhaisalkar,*[,‡] Michael Grätzel,[§] and Nam-Gyu Park*[,†]

[†]School of Chemical Engineering and Department of Energy Science, Sungkyunkwan University, Suwon 440-746, Korea

[‡]Energy Research Institute, Nanyang Technological University, Nanyang Avenue, Singapore 639798

[§]Laboratory for Photonics and Interfaces, Institute of Chemical Sciences and Engineering, School of Basic Sciences, Ecole Polytechnique Fédérale de Lausanne, CH-1015 Lausanne, Switzerland

Supporting Information

ABSTRACT: We report a highly efficient solar cell based on a submicrometer (~0.6 μm) rutile TiO_2 nanorod sensitized with $CH_3NH_3PbI_3$ perovskite nanodots. Rutile nanorods were grown hydrothermally and their lengths were varied through the control of the reaction time. Infiltration of spiro-MeOTAD hole transport material into the perovskite-sensitized nanorod films demonstrated photocurrent density of 15.6 mA/cm^2, voltage of 955 mV, and fill factor of 0.63, leading to a power conversion efficiency (PCE) of 9.4% under the simulated AM 1.5G one sun illumination. Photovoltaic performance was significantly dependent on the length of the nanorods, where both photocurrent and voltage decreased with increasing nanorod lengths. A continuous drop of voltage with increasing nanorod length correlated with charge generation efficiency rather than recombination kinetics with impedance spectroscopic characterization displaying similar recombination regardless of the nanorod length.

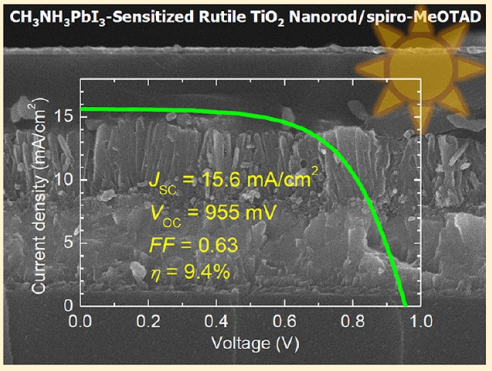

KEYWORDS: *Solid-state dye-sensitized solar cell, perovskite, $CH_3NH_3PbI_3$, nanorod, rutile, impedance spectroscopy*

Invention of dye-sensitized solar cell (DSSC) with a PCE of about 7% in 1991[1] has triggered researches on physics and device technologies of DSSC. As a result, a PCE as high as 12% has been recently achieved using porphyrin-sensitized mesoporous TiO_2 photoanode and cobalt redox electrolyte.[2] Commercialization of electrolyte-containing DSSC structures, however, has been hindered because of concern over the leakage of the liquid electrolyte. Ionic liquid electrolytes or polymer gel electrolytes have been proposed to address potential leakage issues;[3,4] however, the demonstrated PCEs of about 8% are still lower than solvent-laden redox electrolytes. Substitution of liquid redox electrolytes with solid hole transporting materials (HTMs) leads to a solvent-free solid state sensitized heterojunction solar cell.[5] This device has been usually fabricated using a dye-sensitized mesoporous TiO_2 film as an electron transporting layer and a HTM as a hole transporting layer. The PCEs of inorganic chalcogenide- or organic dye-based solid state DSSCs have attained 6−7%;[6,7] whereas, recent reports on solid state DSSCs based on perovskite $CH_3NH_3PbI_{3-x}Cl_x$ (x = 0 or 1) sensitizers have exceeded PCEs of 11%, promising further breakthroughs in this field of study.[8,9]

Mesoporous metal oxide films have been usually adopted for solid-state DSSC; however, difficulty in pore filling has been a persistent issue in such nanoparticulate films because of its labyrinthine mesoporous structure.[10] Nanorod or nanotube structure may be better for pore filling of the HTM materials than the nanoparticulate structure because its open porous structure. Moreover, nanorod or nanotube TiO_2 films were reported to be better in electron transport and recombination behavior than nanoparticulate films in the liquid-based DSSCs.[11,12] Highly crystalline rutile TiO_2 nanorod has been intensively investigated because of its strong advantages, such as easily controllable diameter and length[13] and 2 orders of magnitude higher electron mobility than nanoparticle TiO_2.[14−16] Ordered rutile TiO_2 nanorod sensitized with organic dye was first applied to solid-state DSSC;[17] however, the low PCEs (~2.9%), could possibly be attributed to reduced roughness factor (and reduced dye-loading) yielding lower light harvesting abilities compared to the sintered TiO_2 nanoparticles. This result implied that 1-dimensional nanorod structures were not amenable to low molar extinction coefficient sensitizers despite its many advantages including

Received: January 23, 2013
Revised: April 16, 2013
Published: May 14, 2013

facile infiltration of HTM. One of possible ways to improve the photovoltaic performance of nanorod-based solid state DSSC is to increase total surface area of nanorod structure or to find sensitizers with high light absorption. Recently, we found that absorption coefficient of perovskite $CH_3NH_3PbI_3$ sensitizer was 1 order of magnitude higher than that of the ruthenium-based N719 dye.[18] Moreover, even though the surface coverage of perovskite on TiO_2 was estimated to be only ~28%, photocurrent density nearly doubled compared to almost fully covered N719. Thus, perovskite sensitizers could be considered to be ideally suited for incorporation into nanorod-based solid state DSSCs. Reciprocally, nanorod semiconductor structures are very good candidates for improving the efficiency of photovoltaic devices based on perovskite absorber. Besides the improvement of the charge transport compared to the nanoparticles, tuning the nanorod thickness, length, and density can derive to a better infiltration of both the absorber and the hole transporting material. This is a matter of especial importance for high extinction coefficient absorbers. Considering the excellent absorption proprieties of $CH_3NH_3PbI_3$, a possible decrease of the total surface area of the nanorods compared to the nanoparticles structures will not provoke a significant deterioration of the current. On the contrary, a better distribution of the materials in the semiconductor structure will play a determining role in the enhancement of the charge photogeneration.

Here we report high efficiency solid state DSSC based on rutile TiO_2 nanorods with surface-decorated $CH_3NH_3PbI_3$ perovskite nanocrystals which function as the light absorber. Infiltration of perovskite-adsorbed submicrometer-thick rutile TiO_2 nanorod films with spiro-MeOTAD yielded a strikingly high PCE of 9.4% under AM 1.5G illumination. Dependences of photovoltaic performance and interfacial electronic behavior on the length of rutile TiO_2 nanorods were also investigated.

Figure 1 shows the X-ray diffraction (XRD) spectrum of the vertically grown TiO_2 nanorods on FTO glass substrate, where the diffraction peaks are identified as the rutile phase according to JCPDS 21-1276 data. For the case of rutile TiO_2 powder containing randomly oriented crystals the (110) diffraction intensity is usually highest as can be seen in Figure 1b, which was similarly observed for the rod-shaped rutile TiO_2 nanoparticles.[19] However, in the present case, the (101) diffraction intensity is highest, whereas the (110) peak intensity is noticeably weak. Moreover, the (002) peak is relatively enhanced compared to the randomly oriented powder sample. The highly intense (101) peak along with the enhanced (002) peak in the nanorod film suggests that the rutile crystal grows with (101) plane parallel to the FTO substrate and the nanorods are oriented along the (002) direction.[20,21]

Figure 2 shows plane-view and cross sectional SEM images of the rutile TiO_2 nanorod films and solar cells. The nanorods with rectangular cross section are uniformly distributed on the FTO substrate (Figure 2a–c). At the given temperature of 170 °C, the nanorod dimensions are influenced by the autoclaving process, with length and width increasing with increasing processing time (Figure 2d–f). The dimension of the TiO_2 nanorods was determined to be ~0.5–0.6 μm long and 80 nm wide for 2 h growth, ~1.0–1.2 μm long and 120 nm wide for 2 h and 45 min, and ~1.4–1.6 μm long and 150 nm wide for 3 h and 15 min, where width is estimated from the center of the nanorods (Figure 2d–f). It is worth to remark that nanorod samples used for the FESEM film characterization and device fabrication were from the same synthesis batch but grown on

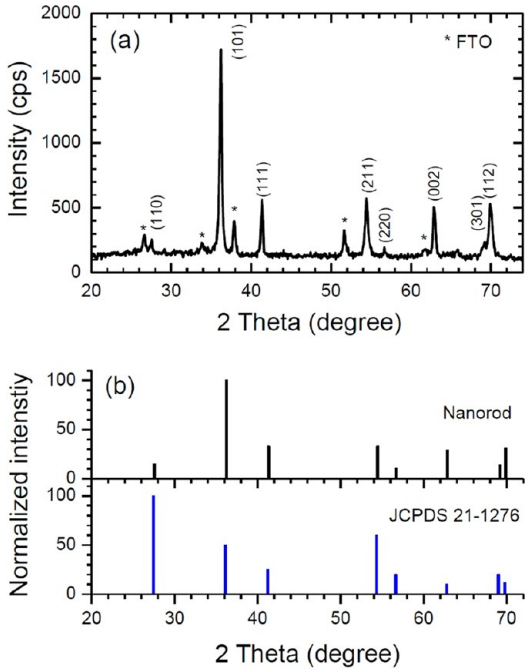

Figure 1. (a) XRD pattern of TiO_2 nanorods grown on FTO glass substrate. (b) Comparison of diffraction intensity between rutile TiO_2 nanorods and the reference JCPDS 21-1276 data (rutile TiO_2 powder).

different substrates, hence minor discrepancies in the nanorod length were observed. Homogeneous and vertically aligned nanorods form at relatively shorter reaction time (Figure 2a) compared with reduced degree of order and alignment observed at longer reaction times (Figures 2b and c). Solid-state DSSC structures viewed by cross-sectional FESEM (Figure 2g–i) indicate infiltration by spiro-MeOTAD in the gap between the nanorods and the top Au electrode is well separated from the photoanode. Pores are relatively well filled by the spiro-MeOTAD for the shorter nanorod film (Figure 2g) compared with the longer nanorod films (Figure 2h and i).

Roughness factor of nanorod films is estimated from the hexagonally close packed model (Figure S1). Assuming that cylindrical nanorods are hexagonally close packed, roughness factor for the film with nanorods having 0.56 μm long ×80 nm wide is calculated to be about 25, which is only 20% of the roughness factor of 124 for the hexagonally close packed spherical nanoparticle (diameter of 20 nm) film with the same thickness of 0.56 μm (see Supporting Information for detailed calculation). Roughness factor is calculated to be about 25, 28, and 38 for 0.56, 0.92 and 1.58 μm nanorods, respectively, which indicates that surface area of nanorod films is not lineally proportional to the length due to simultaneous increase in diameter with increasing the nanorod length. Little change in the roughness factor is therefore correlated with no significant change in absorbance with the nanorod length (Supporting Information Figure S2).

Spin-coated $CH_3NH_3PbI_3$ on the rutile TiO_2 nanorods shows semispherical morphology with an average diameter of ca. 2.5 nm as can be seen in TEM micrograph in Figure 3. Moreover, TiO_2 nanorod surface is not fully covered with $CH_3NH_3PbI_3$ semispheres, which is similarly observed for the case of anatase TiO_2 nanoparticles.[18]

One sun illumination on the solid-state DSSC based on perovskite-sensitized TiO_2 nanorods (0.56 μm) yields a PCE of

dx.doi.org/10.1021/nl400286w | Nano Lett. 2013, 13, 2412–2417

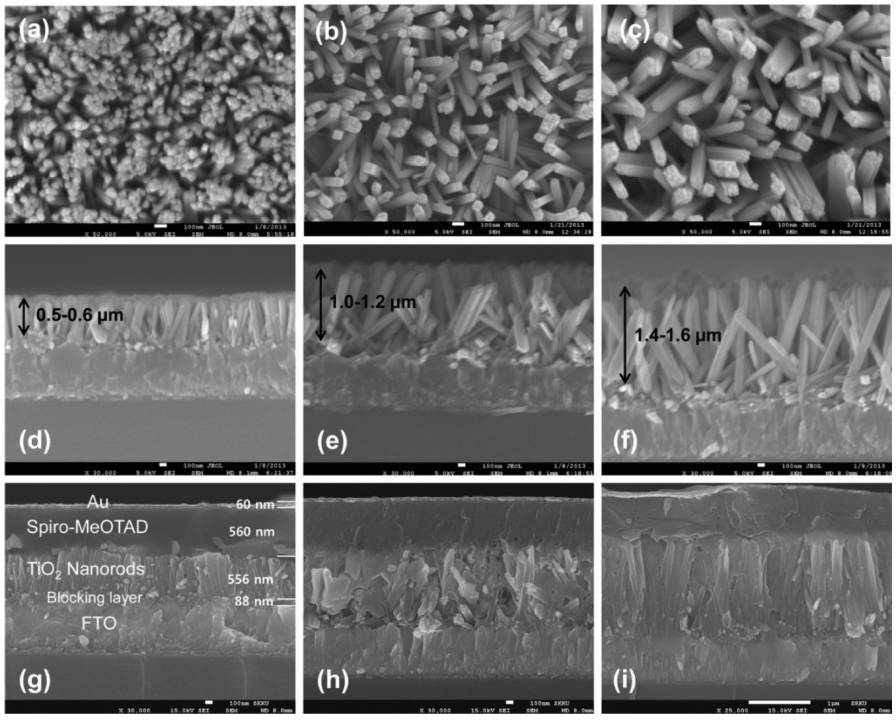

Figure 2. (a–c) Surface and (d–f) cross-sectional FESEM images of rutile TiO_2 nanorods grown on FTO substrate. (g–i) Cross-sectional SEM images of solid state DSSCs based on perovskite $CH_3NH_3PbI_3$-sensitized rutile TiO_2 nanorod photoanode, the spiro-MeOTAD hole transporting layer, and the Au cathode. Scale bars in panels a–h are 100 nm and that in panel i is 1 μm.

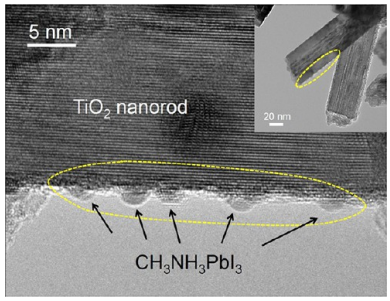

Figure 3. TEM micrograph of $CH_3NH_3PbI_3$ deposited on the surface of TiO_2 nanorod.

9.4% (Figure 4), which results from photocurrent density (J_{sc}) of 15.6 mA/cm^2, open-circuit voltage (V_{oc}) of 955 mV and fill factor of 0.63. IPCE of over 50% is observed at almost entire wavelength range from 400 to 750 nm with a maximum of 71%

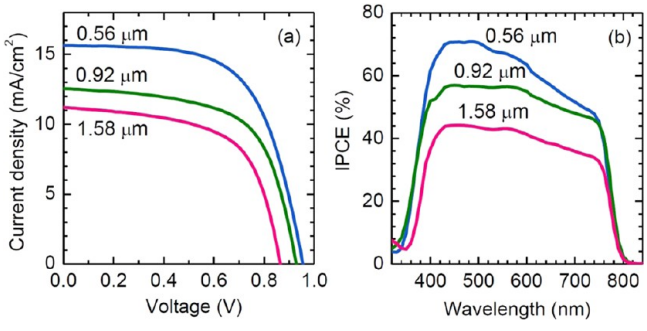

Figure 4. Effect of length of TiO_2 nanorod on (a) current density–voltage curves and (b) IPCE in a solid-state DSSC based on $CH_3NH_3PbI_3$-sensitized rutile TiO_2 nanorod and spiro-MeOTAD.

attained at wavelengths between 420 and 500 nm. The threshold wavelength of 820 nm is related to the band gap of around 1.5 eV for the perovskite.[8] It is noted that high J_{sc} observed in perovskite-sensitized TiO_2 nanorod in spite of low roughness factor is mainly attributable to the high absorption coefficient of the perovskite sensitizer. Molar extinction coefficient of $CH_3NH_3PbI_3$ is about 1.5×10^5 M^{-1} cm^{-1} at 550 nm,[18] which is 2–3 times higher than those of organic dyes such as D149 with 6.9×10^4 M^{-1} cm^{-1} at 526 nm[22] and Y123 with 5.3×10^4 M^{-1} cm^{-1} at 532 nm.[23]

Effect of the nanorod length on photovoltaic performance was investigated, where photovoltaic performance is degraded with increasing nanorod length (Figure 4 and Table 1). With

Table 1. Photovoltaic Parameters of Short-Circuit Photocurrent Density (J_{sc}), Open-Circuit Voltage (V_{oc}), Fill Factor (FF), and Power Conversion Efficiency (η), Depending on TiO_2 Nanorod Length

TiO_2 nanorod length (μm)	J_{sc} (mA/cm^2)	V_{oc} (mV)	FF	η (%)	area (cm^2)
0.56	15.6	955	0.63	9.4	0.215
0.92	12.6	929	0.62	7.3	0.206
1.58	11.2	865	0.61	5.9	0.193

increasing the nanorod length, J_{sc} and V_{oc} decrease as shown in Table 1, with a corresponding decrease in PCE from 9.4% (0.56 μm) to 7.3% (0.92 μm) and to 5.9% (1.58 μm). IPCE in Figure 4b shows relatively higher IPCE for the 0.56 μm-long TiO_2 nanorod at wavelength ranging between 420 and 600 nm, which indicates that the shorter nanorods utilize short wavelength light more efficiently than the longer nanorods.

The decrease in J_{sc} with increasing the nanorod length is likely to be related to either amount of the adsorbed perovskite

dx.doi.org/10.1021/nl400286w | Nano Lett. 2013, 13, 2412–2417

or pore filling fraction (PFF). J_{sc} is proportional to IPCE, where IPCE is the product of light harvesting efficiency (η_{lh}), electron injection efficiency ($\eta_{e\text{-}inj}$), hole injection efficiency ($\eta_{h\text{-}inj}$), and charge collection efficiency (η_{cc}), IPCE = $\eta_{lh} \times \eta_{e\text{-}inj} \times \eta_{h\text{-}inj} \times \eta_{cc}$. η_{lh} is determined by absorption of sensitizer, where higher absorbance due to larger amount of sensitizer is expected to lead to higher η_{lh}. Since little difference in absorbance is observed for different length (Figure S2), light harvesting efficiency seems to be similar and is irrelevant to the change in J_{sc}. $\eta_{e\text{-}inj}$ is thought to be similar regardless of the nanorod length because interfacial property between the perovskite and the rutile TiO_2 surface will be identical. On the other hand, $\eta_{h\text{-}inj}$ is directly affected by PFF of HTM. It was found that a significant increase in J_{sc} was observed upon increasing PFF,[24] which is related to the improved hole injection. PFF is estimated from the HTM overlayer thickness (see Supporting Information for detailed calculation). It is usually found that the thickness of HTM overlayer was gradually reduced with increasing film thickness as long as all the spin-coating parameters were fixed.[25] However, the HTM overlayer thickness increases with increasing the length of nanorod despite the same HTM spin-coating condition, as shown in SEM images in Figure 2g–i. The HTM overlayer thickness increases from 560 nm for the 0.56 μm-long nanorod to 620 and 750 nm for the 0.92 and 1.58 μm-long nanorods, respectively, which is indicative of decrease in PFF with increasing the nanorod length. Figure 5 shows a schematic

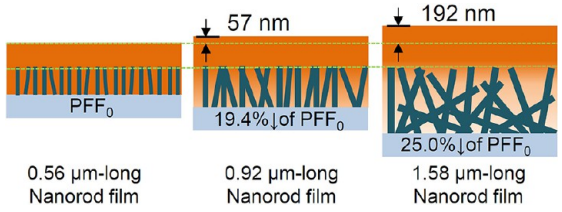

Figure 5. Schematic drawing showing the effect of HTM overlayer thickness on the PFF. PFFs for 0.92 μm- and 1.58 μm-long nanorod films were estimated relative to PFF for 0.56 μm-long nanorod film (PFF_0).

drawing of nanorod film structure depending on the nanorod length, based on SEM images in Figure 2d–f. Decrease in PFF for the longer nanorods is attributed to the tilted nanorods compared with the vertical alignment of shorter nanorod. The poor PFF leaves voids in the bottom of the films as shown in Figure 2h and i. As a result, PFFs of the films with 0.92 μm- and 1.58 μm-long nanorods are about 19% and 25% lower than that of the 0.56 μm-long nanorod (Supporting Information Table S1). Thus, decrease in J_{sc} with increasing the nanorod length is closely related to the lowered PFF, associated with nanorod alignment.

Charge recombination rate is similar but electron diffusion coefficient is faster for the longer nanorod (Supporting Information Figure S3). Neverthless, J_{sc} is lower for the longer nanorod than for the shorter one, which underlines that dependence of J_{sc} on the nanorod length is mainly related to $\eta_{h\text{-}inj}$ which is investigated by PFF. The inverse dependence between photovoltaic performance and nanorod length bears a similarity with previous observations in anatase nanoparticle-based devices,[8] where change of V_{oc} with thickness was explained by analyzing impedance spectroscopy (IS). To elucidate the differences in the performance for the nanorod-based perovskite-sensitized solid state devices, IS characterization was carried out.

The cell response under one sun illumination conditions was analyzed for 0.56 and 1.58 μm nanorod devices at different applied DC voltages. The obtained spectra (Figure 6a) present

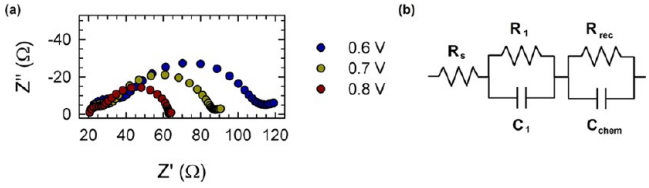

Figure 6. (a) IS spectra for solar cell made with the 0.56 μm-long TiO_2 nanorod film measured under one sun illumination, where the applied DC voltage was 0.6, 0.7, and 0.8 V. (b) Equivalent circuit employed to fit the spectra.

two arcs and a low frequency feature. The latter is attributed to slow charge transport, does not have direct relevance to the device physics, and is thus not included in the fitting and subsequent analysis. The first arc, at higher frequencies, is related to the hole transport and extraction in the cathode and has a similar effect in both shorter and longer nanorod devices. The main arc is due to the combination of the recombination resistance (R_{rec}) and the chemical capacitance of the film (C_μ).[26] The shape of this arc has does not indicate any significant issues in charge transport and may thus be interpreted as an efficient minority carrier transport for all the employed films, regardless of their thicknesses. As a consequence, in order to calculate the parameters, the typical transmission line model employed for dye solar cells[27] may be simplified to the equivalent circuit shown in Figure 6b.

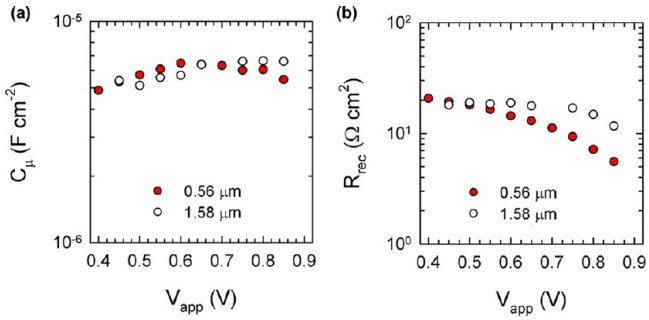

Figure 7. (a) Chemical capacitance and (b) recombination resistance resulting from the IS measurements fitting for different applied bias at one sun illumination.

The results of C_μ and R_{rec} are shown in Figure 7. The C_μ is associated with the homogeneous accumulation of minority carriers (eq 1)[28]

$$C_\mu^{(n)} = Lq^2 \frac{dn}{dE_{Fn}} \quad (1)$$

where the capacitance is given by unit of area, n is the carrier density, and E_{Fn} is the Fermi level for electrons in the film. As it has been previously reported for these type of devices,[27] C_μ does not increase as much as in anatase nanoparticle-based perovskite-sensitized solid state devices.[8] The identical C_μ for both devices indicates that the same energy levels are being

dx.doi.org/10.1021/nl400286w | Nano Lett. 2013, 13, 2412–2417

filled and that the energy bands do not exhibit any shifts as the nanorod lengths increase. R_{rec} presents also a similar behavior for both devices (Figure 7b), with slightly higher values for the longer nanorods. It is worthwhile to note that increase in nanorod thickness accompanies any increase in its length (Figure 2). In this analysis the measured resistance and capacitance characteristic of the device are given per unit geometrical area. Since the nanorods diameter also changes depending on their length, to account for this nanostructure architectural effect, R_{rec} and C_{μ} were normalized to the effective surface area and volume respectively (see Supporting Information). With this normalization, the results (Supporting Information Figure S4) reproduce the observed tendency, with both C_{μ} and R_{rec} showing very little differences for nanorods with 0.56 or 1.58 μm lengths. This is an indication that the different configurations have an insignificant effect on the recombination rate. This result is consistent, on one hand, with the similar shape of the three current−voltage curves, and on the other, with the differences of V_{oc} observed (Figure 4), which are directly related to the different charge generation. All these facts point to a similar recombination process in the analyzed devices and also confirm that the main effect of the nanorod length in the studied solar cells is on the charge generation.

In conclusion, we fabricated high efficiency solid-state DSSC based on submicrometer-thick rutile TiO_2 nanorod films whose surface was sensitized with perovskite $CH_3NH_3PbI_3$ nanodots. Despite the significant reduction in surface area compared to nanoparticle films, demonstrated J_{sc} was as high as over 15 mA/cm^2 because of high absorption coefficient of perovskite $CH_3NH_3PbI_3$. J_{sc} was found to be influenced by nanorod ordering, associated with pore filling fraction. Well-ordered 1-D structure of shorter nanorod film was better for infiltration of spiro-MeOTAD than the longer nanorod film with disordered structure, which resulted in higher photovoltaic performance. Eventually, a PCE of 9.4% was achieved with ∼0.6 μm-thick rutile TiO_2 nanorod film under one sun illumination. This data is so far the highest efficiency for the rutile TiO_2 nanorod based DSSCs. Since comparative studies on photovoltaic behavior and performance between anatase and rutile TiO_2 nanorods is expected to provide more advanced information, attempt to fabricate and study the solid state perovskite-sensitized solar cells based on well-defined anatase TiO_2 nanorod is underway.

Materials and Methods. *Synthesis of Perovskite Sensitizer.* The perovskite sensitizer $CH_3NH_3PbI_3$ was prepared according to the reported procedure.[8] A hydroiodic acid (30 mL, 0.227 mol, 57 wt.% in water, Aldrich) and methylamine (27.8 mL, 0.273 mol, 40% in methanol, TCI) were stirred in the ice bath for 2 h. After it was stirred at 0 °C for 2 h, the resulting solution was evaporated at 50 °C for 1 h to precipitate CH_3NH_3I. The precipitate was washed three times with diethyl ether and dried under vacuum and used without further purification. To deposit $CH_3NH_3PbI_3$ on the rutile TiO_2 nanorod film, a precursor solution was prepared by mixing the readily synthesized CH_3NH_3I (0.395 g) and PbI_2 (1.157 g, 99% Aldrich) in γ-butyrolactone (2 mL, >99% Aldrich) at 60 °C for overnight under stirring.

Preparation of Rutile TiO_2 Nanorods. TiO_2 nanorods were grown on the FTO-coated dense TiO_2 layer (i.e., blocking layer) substrates. The blocking layers were grown on freshly cleaned FTO glasses as per previously reported procedure.[8] The blocking layer coated substrates were used to grow the TiO_2 nanorods. TiO_2 nanorods were prepared via hydrothermal synthesis method following the reported procedure.[15] In brief, the hydrothermal synthesis was carried out in a stainless steel autoclave with Teflon liner of 50 mL capacity. In a typical synthesis step, 20 mL of 37% hydrochloric acid was added in the 20 mL of deionized water and sonicated for 5 min. Subsequently 0.7 mL of titanium(IV) n-butoxide (99%, Acros Organics-Fisher Scientific) was added and further sonicated for 5 min. Four pieces of FTO with blocking layer were used as substrates (2.5 cm ×2.4 cm) and positioned tilted inside the Teflon liner with the active layer facing the wall. The above-mentioned precursor mixture was then transferred into autoclave containing the substrates. The properly sealed autoclave was placed inside the oven preheated to 170 °C. The reaction time was set to 2 h, 2 h 45 min, and 3 h 15 min to get the desired TiO_2 nanorod length, that is, 0.5−0.6, 1.0−1.2, and 1.4−1.6 μm, respectively. The autoclave was then naturally cooled to room temperature. The substrates were taken out from the autoclave, rinsed thoroughly, and annealed at 300 °C in air prior to use.

Solar Cell Fabrication and Characterization. The rutile TiO_2 nanorod films were coated with perovskite precursor solution, followed by heating at 100 °C for 15 min. The yellow color film turned black during heating. The composition of hole transport material (HTM) was 0.140 M 2,2′,7,7′-tetrakis-(*N*,*N*-di-*p*-methoxyphenyl-amine)-9,9′-spirobifluorene (spiro-MeO-TAD, Merck), 0.064 M bis(trifluoromethane)sulfonimide lithium salt (LiTFSI, 99.95%, Aldrich), and 0.198 M 4-*tert*-butylpyridine (TBP, 96%, Aldrich) in the mixed solvent of chlorobenzene (99.8%, Aldrich) and acetonitrile (99.8%, Aldrich) (chlorobenzene/acetonitrile =1: 0.1 v/v). The $CH_3NH_3PbI_3$-sensitized TiO_2 nanorod films were coated with HTM solution using spin-coating method at 3000 rpm. For the counter electrode, a 60 nm-thick Au was deposited on the top of the HTM over layer by a thermal evaporation, where Au evaporated under ∼10^{-6} Torr vacuum condition. The active area was measured by a digital camera (DCMe 500) and an image analysis program (Leopard 2009). The phases of the hydrothermally grown nanorods were investigated by X-ray diffraction (XRD, Bruker-AXS D8 Advance). A field-emission scanning electron microscope (FE-SEM, Jeol JSM 6700F) was used to investigate plane and cross-sectional morphologies of the nanorods and the solid state devices. A high-resolution transmission electron microscope (HR-TEM, Jeol, JEM-2100F) was used to confirm the morphology of $CH_3NH_3PbI_3$ deposited on TiO_2 nanorods. Photocurrent and voltage were measured by a solar simulator (Oriel Sol 3A class AAA) equipped with a 450 W xenon lamp (Newport 6279NS) and a Keithley 2400 source meter. The NREL-calibrated Si solar cell with KG-2 filter was used to adjust light intensity into one sun illumination (100 mW/cm^2). A black aperture mask was attached during photocurrent and voltage measurement.[29,30]

Impedance Spectroscopy. IS measurements were carried out under one sun light intensity with an Autolab 302 N, with different DC bias potentials from 100 to 1000 mV. The applied voltage perturbation had an AC amplitude of 20 mV (rms) with a frequency from 1 MHz to 0.1 Hz. The spectra were fitted using Z-View software.

■ ASSOCIATED CONTENT

Ⓢ Supporting Information

Roughness factor calculation, UV−vis spectra of $CH_3NH_3PbI_3$-sentized nanorod films, evaluation of pore filling fraction, transient photocurrent and photovoltage measurement, and

impedance spectroscopy characterization. This material is available free of charge via the Internet at http://pubs.acs.org.

AUTHOR INFORMATION

Corresponding Author

*N.G.P.: Tel +82-31-290-7241, fax +82-31-290-7272, e-mail: npark@skku.edu. S.M.: Tel +65-6790-4626, fax +65-6790-9081, e-mail subodh@ntu.edu.sg.

Notes

The authors declare no competing financial interest.

ACKNOWLEDGMENTS

This work was supported by the National Research Foundation of Korea (NRF) grant funded by the Ministry of Science, ICT & Future Planning (MSIP) under contracts NRF-2010-0014992, NRF-2012M1A2A2671721, and NRF-2012M3A6A7054861 (the Global Frontier R&D Program on Center for Multiscale Energy System), and the Korea Institute of Energy Technology Evaluation and Planning (KETEP) grant funded by the Ministry of Trade, Industry & Energy (MOTIE) under contract No. 20103020010010. H.-S.K and J.-W.L were supported in part by global Ph.D. fellowship funded by NRF (NRF-2011-0008467, NRF-2011-0008000). This work was also supported by National Research Foundation (NRF) Competitive Research, Programs (CRP) under projects NRF-CRP5-2009-04 and NRFCRP4200803.

REFERENCES

(1) O'Regan, B.; Grätzel, M. *Nature* **1991**, *353*, 737−740.
(2) Yella, A.; Lee, H.-W.; Tsao, H. N.; Yi, C.; Chandiran, A. K.; Nazeeruddin, M. K.; Diau, E. W.-G.; Y, C.-Y.; Zakeeruddin, S. M.; Grätzel, M. *Science* **2011**, *334*, 629−634.
(3) Wang, P.; Zakeeruddin, S. M.; Moser, J.-E.; Humphry-Baker, R.; Grätzel, M. *J. Am. Chem. Soc.* **2004**, *126*, 7164−7165.
(4) Lee, K. S.; Jun, Y.; Park, J. H. *Nano Lett.* **2012**, *12*, 2233−2237.
(5) Bach, U.; Lupo, D.; Comte, P.; Moser, J.-E.; Weissörtel, F.; Salbeck, J.; Spreitzer, H.; Grätzel, M. *Nature* **1998**, *395*, 583−585.
(6) Chang, J. A.; Im, S. H.; Lee, Y. H.; Kim, H.; Lim, C.-S.; Heo, J. H.; Seok, S. I. *Nano Lett.* **2012**, *12*, 1863−1867.
(7) Burschka, J.; Dualeh, A.; Kessler, F.; Baranoff, E.; Cevey-Ha, N. -L.; Yi, C.; Nazeeruddin, M. K.; Grätzel, M. *J. Am. Chem. Soc.* **2011**, *133*, 18042−18045.
(8) Kim, H.-S.; Lee, C.-R.; Im, J.-H.; Lee, K.-B.; Moehl, T.; Marchioro, A.; Moon, S.-J.; Humphry-Baker, R.; Yum, J.-H.; Moser, J.-E.; Grätzel, M.; Park, N.-G. *Sci. Rep.* **2012**, *2*, 591.
(9) Lee, M. M.; Teuscher, J.; Miyasaka, T.; Murakami, T. N.; Snaith, H. J. *Science* **2012**, *338*, 643−647.
(10) Snaith, H. J.; Humphry-Baker, R.; Chen, P.; Cesar, I.; Zakeeruddin, S. M.; Grätzel, M. *Nanotechnology* **2008**, *19*, 424003.
(11) Kang, S. H.; Choi, S.-H.; Kang, M. S.; Kim, J -Y.; Kim, H.-S. *Adv. Mater.* **2008**, *20*, 54−58.
(12) Zhu, K.; Neale, N. R.; Miedaner, A.; Frank, A. J. *Nano Lett.* **2007**, *7*, 69−74.
(13) Liao, Y.; Que, W.; Jia, Q.; He, Y.; Zhang, J.; Zhong, P. *J. Mater. Chem.* **2012**, *22*, 7937−7944.
(14) Feng, X.; Shankar, K.; Varghese, O. K.; Paulose, M.; Latempa, T. J.; Grimes, C. A. *Nano Lett.* **2008**, *8*, 3781−3786.
(15) Liu, B.; Aydil, E. S. *J. Am. Chem. Soc.* **2009**, *131*, 3985−3990.
(16) Hendry, E.; Koeber, M.; O'Regan, B.; Bonn, M. *Nano Lett.* **2006**, *6*, 755−759.
(17) Wang, M.; Bai, J.; Formal, F. L.; Moon, S.-J.; Cevey-Ha, L.; Humphry-Baker, R.; Gratzel, C.; Zakeeruddin, S. M.; Grätzel, M. *J. Phys. Chem. C* **2012**, *116*, 3266−3273.
(18) Im, J.-H.; Lee, C.-R.; Lee, J.-W.; Park, S.-W.; Park, N.-G. *Nanoscale* **2011**, *3*, 4088−4093.
(19) Park, N. G.; Schlichtho1rl, G.; van de Lagemaat, J.; Cheong, H. M.; Mascarenhas, A.; Frank, A. J. *J. Phys. Chem. B* **1999**, *103*, 3308−3314.
(20) Zhang, F.; Liu, X. *Thin Solid Films* **1998**, *326*, 171−174.
(21) Nayak, J.; Prabakar, K.; Park, J. W.; Kim, H. *Electrochim. Acta* **2012**, *6*, 44−49.
(22) Ito, S.; Zakeeruddin, S. M.; H-Baker, R.; Liska, P.; Chavet, R.; Comte, P.; Nazeeruddin, M. K.; Pechy, P.; Takata, M.; Miura, H.; Uchida, S.; Grätzel, M. *Adv. Mater.* **2006**, *18*, 1202−1205.
(23) Taso, H. N.; Yi, C.; Moehl, T.; Yum, J.-H.; Zakeeruddin, S. M.; Nazeeruddin, M. K.; Grätzel, M. *ChemSusChem.* **2011**, *4*, 591−594.
(24) M-Kyriazi, J.; Ding, I.-K.; Marchioro, A.; Punzi, A.; Hardin, B. E.; Burkhard, G. F.; Tetreault, N.; Grätzel, M.; Moser, J.-E.; McGehee, M. D. *Adv. Energy Mater.* **2011**, *1*, 407−414.
(25) Ding, I.-K.; Tetreault, N.; Brillet, J.; Hardin, B. E.; Smith, E. H.; Rosenthal, S. J.; Sauvage, F.; Grätzel, M.; McGehee, M. D. *Adv. Funct. Mater.* **2009**, *19*, 2431−2436.
(26) Mora-Seró, I.; Bisquert, J.; Fabregat-Santiago, F.; Garcia-Belmonte, G.; Zoppi, K.; Y., D.; Proskuryakov, Y.; Oja, I.; Belaidi, A.; Dittrich, T.; Tena-Zaera, R.; Katty, A.; Lévy-Clement, C.; Barrioz, V.; Irvine, S. J. C. *Nano Lett.* **2006**, *6*, 640.
(27) Fabregat-Santiago, F.; Garcia-Belmonte, G.; Mora-Seró, I.; Bisquert, J. *Phys. Chem. Chem. Phys.* **2011**, *13*, 9083−118.
(28) Bisquert, J. *Phys. Chem. Chem. Phys.* **2003**, *5*, 5360−5364.
(29) Park, J.; Koo, H.-J.; Yoo, B.; Yoo, K.; Kim, K.; Choi, W.; Park, N.-G. *Sol. Energy Mater. Sol. Cells* **2007**, *91*, 1749−1754.
(30) Lee, G.-W.; Kim, D. H.; Ko, M. J.; Kim, K. K.; Park, N.-G. *Sol. Energy* **2010**, *84*, 418−425.